Widespread carbon-bearing materials on near-Earth asteroid (101955) Bennu

Science
AAAS

Accepted Manuscript

Widespread carbon-bearing materials on near-Earth asteroid (101955) Bennu

Amy A. Simon[1*], Hannah H. Kaplan[2], Victoria E. Hamilton[2], Dante S. Lauretta[3], Humberto Campins[4], Joshua P. Emery[5], M. Antonietta Barucci[6], Daniella N. DellaGiustina[3], Dennis C. Reuter[1], Scott A. Sandford[7], Dathon R. Golish[3], Lucy F. Lim[1], Andrew Ryan[3], Benjamin Rozitis[8], Carina A. Bennett[3]

Affiliations:

[1]Solar System Exploration Division, NASA Goddard Space Flight Center, Greenbelt, MD, USA.

[2]Southwest Research Institute, Boulder, CO, USA.

[3]Lunar and Planetary Laboratory, University of Arizona, Tucson, AZ, USA.

[4]Department of Physics, University of Central Florida, Orlando, FL, USA.

[5]Department of Astronomy and Planetary Sciences, Northern Arizona University, Flagstaff, AZ, USA.

[6]Laboratoire d'Etudes Spatiales et d'Instrumentation en Astrophysique, Observatoire de Paris, Université Paris Sciences & Lettres, Centre national de la recherche scientifique, Université de Paris, Sorbonne Université, 92195 Meudon, France

[7]NASA Ames Research Center, Moffett Field, CA, USA.

[8]School of Physical Sciences, The Open University, Milton Keynes, UK.

*Correspondence to: amy.simon@nasa.gov.

Abstract: (101955) Bennu is a dark, Earth orbit-crossing, asteroid thought to be assembled from the fragments of an ancient collision. Spatially-resolved visible and near-infrared spectra of Bennu provide details about its surface properties and composition. In addition to a hydrated phyllosilicate band, we detect a ubiquitous 3.4-micron absorption feature, which we attribute to a mix of organic and carbonate materials. The shape and depth of this absorption feature vary across Bennu's surface, spanning the range seen among similar main-belt asteroids. Its distribution does not correlate with the temperature, reflectance, spectral slope, or hydrated minerals although those characteristics correlate with each other in some cases. The deepest 3.4-micron absorptions occur on individual boulders. The variations may be due to differences in abundance, recent exposure, or space weathering.

Main Text:

Asteroid (101955) Bennu is a dark, near-Earth asteroid averaging 4.4% reflectance (*1*), thought to be the collisional remnant of a much larger object in the main asteroid belt (*2*). Bennu is classified as a C-complex asteroid – bodies with low reflectance and spectral similarities with carbonaceous chondrite meteorites, so expected to have high carbon content (*3*). Specifically, Bennu belongs to a subgroup of the C-complex, the B-types, which have bluer spectra (*4*) and are thought to have silicates, hydrated minerals, organic molecules, magnetite, and sulfides on their surfaces (*5*).

Launched in 2016, the Origins, Spectral Interpretation, Resource Identification, and Security–Regolith Explorer (OSIRIS-REx) spacecraft is designed to return a sample of carbonaceous material from Bennu for laboratory analysis (*6*). One of the mission objectives is to compare ground-based Bennu data with the resolved surface to help interpret unresolved observations of other asteroids (*6*). Detailed spatial and spectral maps will also be required to tie the returned sample to its local geologic context.

The B-type asteroids are sub-divided based on their visible to near-infrared (near-IR) spectral slopes, with some bluer objects similar to (2) Pallas, some redder objects similar to (24) Themis, and others in the continuum of spectral slopes between them (*7*). Each of these visible to near-IR spectral slopes can be matched with analogous carbonaceous chondrite meteorites, which show various degrees of aqueous and thermal alteration (*5*). Based on these meteorite comparisons, it has been proposed that the redder-sloped B-types are the most water-rich, similar to the CM class of chondrites, and the bluer-sloped B-types are dry and heated or thermally metamorphosed, similar to the CK4 class of chondrites (*5*). Prior to the OSIRIS-REx spacecraft's arrival, one of the closest spectral matches to Bennu's blue spectral slope (at < 1.5 μm) was a carbonaceous chondrite which shows signs of having been aqueously altered then heated and dehydrated (*8*). However, global spectra acquired during the spacecraft's approach to Bennu showed a 2.7-μm absorption band, indicating hydrated minerals, with a shape more similar to that of the aqueously-altered CM chondrites (*9*).

Bennu is thought to be a member of either the (142) Polana or the (495) Eulalia collisional families; asteroids who appear to originate from a common source in the main asteroid belt between Mars and Jupiter (*10, 11*). Both Polana and Eulalia reside in the main belt and have spectra that indicate they are members of the C-complex (*12*). The Hayabusa2 spacecraft has

visited and sampled the near-Earth asteroid (162173) Ryugu, which is also likely to be a member of the Polana or Eulalia families, but is classified as a near-Earth Cb-type asteroid, a different spectral subgroup of the C-complex (*13*). Spatially resolved spectra from Hayabusa2 indicate that Ryugu has a weaker global 2.7-μm hydration feature than Bennu. On Ryugu the band varies only slightly (7-10% band depth) across the surface which is consistent with thermal processing (*14*). Other asteroid families, such as the (24) Themis family, show spectral diversity among their members and evidence of material separation, possibly into rock and ice - likely enough to produce aqueous alteration (*15*). Similar processing may have occurred in the parent body of Bennu. Bennu is a rubble-pile asteroid, an agglomeration of collision fragments, that was ejected from the main asteroid belt and migrated to its final near-Earth orbit. Global maps of Bennu's spectral chacrteristics are required to understand its relationship to Ryugu and their parent population, as well as to the broader classes of B- and C-type asteroids.

In 2019, the OSIRIS-REx mission completed a campaign of close-proximity observation of Bennu to determine suitable sites for sample collection, which is planned in 2020 (*6*). The OSIRIS-REx Visible and InfraRed Spectrometer (OVIRS) acquired global surface data from 0.4 to 4.3 μm at multiple phase angles (*16*). Visible wavelengths are used to determine the overall color variations across Bennu's surface and its mineral content, whereas the near IR is sensitive to surface temperature and compositional variations. The OVIRS near-IR coverage near 2.7 μm has been used to detect the global presence of hydrated minerals (*9*), and the region from 3.2 to 3.6 μm is sensitive to carbonate (CO_3^{2-} stretching or vibration) and organic (C-H stretching) absorption bands.

We investigate the spectrum of Bennu using OVIRS observations and search for evidence for absorption bands attributable to carbon-bearing materials. Our goal is to compare the shape of any carbon-bearing absorption features with spectra of other C-complex asteroids and determine the surface distribution of carbon-bearing materials.

Observations and mapping

We use data from the Equatorial Stations subphase (25 April to 6 June 2019) of the OSIRIS-REx Detailed Survey phase, which ran from 7 March through 6 June 2019. The subphase was composed of data collection from seven spacecraft stations, each positioned close to the equator at a different local solar time and ~5 km above the surface (*6*). As OVIRS is a point spectrometer, with a circular 4-mrad field of view, each spectrum covers all wavelengths simultaneously for a spot on the surface (*16*). At each local solar time, the spacecraft nodded along lines of constant longitude at ~2 mrad s^{-1} to achieve nearly global OVIRS coverage as the asteroid rotated below. Although OVIRS observed most latitudes and longitudes at each station, the individual spots were not centered at the exact same locations from station to station. The spot spatial resolution was ~20-m cross-track and 30-m along-track at the equator. Surface projection increase the along-track spot size at higher latitudes and local surface slopes also cause the resolution to vary. From these data, we produced global OVIRS maps at ~600-m^2 equatorial areal resolution from the stations at 10:00 am, 12:30 pm, and 3:00 pm local solar time, as these have the highest available solar illumination and maximum surface temperatures.

From 4 to 27 October 2019, the spacecraft conducted lower-altitude reconnaissance flyovers of four candidate sample sites and surrounding context regions, scanning each area of interest at a

range of 1 to 1.3 km (*6*). Reconnaissance flyovers occurred when Bennu was at larger distance from the Sun than during the Detailed Survey, and therefore solar illumination was lower; longer exposure times were used to compensate. The resulting OVIRS spatial resolution was ~4 to 5 m cross-track and ~7 to 10 m along-track, plus the surface projection effects at the higher latitudes. We produced spectral maps of these smaller regions at ~60-m^2 areal resolution.

Globally averaged spectra

Global spectra were calculated for each Detailed Survey equatorial spectral mapping station by averaging all OVIRS spots that were fully on the surface; there are 6189, 7193, and 6877 spectra for 10:00 am, 12:30 pm, and 3:00 pm, respectively. Although not identical to a full-disk spectrum due to the fixed local time, the averages include emission angles from latitudes all the way to the poles. In the 12:30 pm data, Bennu shows a weak global absorption feature from 3.2 to 3.6 μm (hereafter, the 3.4-μm feature) which we attribute to carbonate and organic materials (Fig. 1B). This absorption feature was not detectable in full-disk, unresolved OVIRS spectra, taken when Bennu only filled ~40% of the field of view and the surface was warmer owing to closer proximity to the Sun (*9*). Spatially-resolved data sets were also acquired in March 2019, very close to Bennu's perihelion. These contain hits of a 3.4-μm absorption feature, but the band depth was likely affected by thermal fill-in, an effect whereby greater thermal emission at high temperatures increases the thermal flux at the band wavelength, thereby weakening absorption features (*17*). Those spectra were also noisier at long wavelengths > 3 μm, owing to higher instrument detector temperatures.

Bennu's globally averaged 3.4-μm absorption feature, as observed during the Detailed Survey, is distinct from that seen on other C-complex asteroids (Fig. 1). Previous observations of a 3.4-μm feature in other disk-integrated asteroid spectra, including (24) Themis and Themis-like asteroids, have been attributed primarily to aliphatic organic molecules (e.g., *18-20*). However, ground-based observations of (1) Ceres and Ceres-like asteroids have revealed a strong 3.4-μm feature that was instead primarily attributed to carbonates, as it was accompanied by a detection of the 3.9-μm carbonate band (*20, 21*). Several main-belt asteroids display variability between 3.2 and 3.6 μm, indicating potential compositional variation, though the bands variations are uncertain for (704) Interamnia and (121) Hermione (Fig. 1A) (*18, 22*). However, in individual spot spectra, Bennu has absorption band shapes between 3.2 and 3.6 μm that are similar to those of Themis and Ceres, along with other main-belt asteroids (Fig. 1B).

We also produced a globally averaged thermal infrared spectrum using data from the OSIRIS-REx Thermal Emission Spectrometer (OTES) (*23*), acquired during the Detailed Survey phase, to search for spectral features that could be attributable to carbon in organics and/or carbonates. However, other minerals exhibit features in the same spectral region, complicating our interpretation. The radiometric performance of OTES is degraded at >1300 cm^{-1} ($\lesssim$7.7 μm) and at surface temperatures lower than 325 K (*23*), requiring us to co-add spectra to maintain an adequate signal-to-noise ratio (Fig. S1) (*24*). This prevents us from obtaining detailed spatial distribution information for comparison with the OVIRS observations made at four times the areal resolution. We therefore limit our analyses to the OVIRS data only.

Feature repeatability

With repeated coverage over some areas of Bennu's surface, we investigated the effects of phase angle on spectral shape to determine whether the absorption is an observational or processing artifact. The globally averaged spectra from the three local solar times are shown in Fig. 2A. A similar 3.4-μm band shape is seen in each average spectrum, though at 12:30 pm and 3:00 pm, the feature is slightly deeper near 3.45 μm and has more absorption < 3.3 μm than at 10:00 am. There is no apparent thermal emission fill-in in the absorption band at any phase angle because the average surface temperatures were low (328K at 12:30 pm); however individual hot surface locations become very noisy in the 3:00 pm spectra. Using the average surface temperatures, reflectance, and solar range–corrected flux for each observation, the radiance contribution from reflected solar light at 3.4 μm is ~31%, 22%, and 15% for 10:00 am, 12:30 pm, and 3:00 pm, respectively. However, the absolute reflected solar radiance at 12:30 pm is nearly twice that at 10:00 am and 3:00 pm, resulting in the highest signal-to-noise after thermal tail subtraction (Fig. S2) (*24*).

We also investigated feature repeatability on a regional scale. Using the regions with higher resolution observations (Fig. 2B), we averaged several overlapping spots together obtain a close match to the spatial resolution of each Detailed Survey map (though not identical). Two overlapping spots in each observation cover ~900 m^2, and the afternoon spectra again have a deeper band than 10:00 am spectra, but spectral shapes are similar for each observation. We also compared the average of all high-spatial-resolution spots over an area with the corresponding low-spatial-resolution spectrum (Fig. 2, C and D). Although the spectra were taken at different local solar times, differences between the resulting spectra are <0.5%, indicating that phase angle does not appreciably affect the band depth or shape.

Global surface distribution

To map the distribution of the absorption feature across the surface, we used the 12:30 pm spectra as they have the highest signal-to-noise ratio and fewest shadows. From those data, we calculated the band area (band depth integrated from 3.2 to 3.6 μm), mapped it onto the surface of a 3D shape model of Bennu (*25*), and overlaid the results on an OSIRIS-REx Camera Suite (OCAMS) base map with 5-cm spatial resolution (*26, 27*) (Fig. 3A). Band area was chosen, rather than single-channel band depth, to cover the range of spectral shapes which could arise due to different carbonates or organics (*28*).

The map in Fig. 3A shows that carbon-bearing material is spread over 98% of Bennu's surface, with band areas varying from 0.12 to 0.82 % μm, but in no discernible large-scale pattern; 98% of the surface between ±50° latitude shows a band depth >1% at 3.42 μm and 32% of the surface has an absorption ≥ 2%. Most other surface parameters, such as 12:30 pm surface temperature, 0.55-μm reflectance, or visible spectral slope (Fig. 3, B to D), align with surface features: the darkest boulders and blanketed areas (lowest 0.55-μm reflectance) tend to be the hottest and have the shallowest hydration band at 2.74 μm. The boulders appear to have low thermal inertia, high thermal roughness, and usually a redder spectral slope (*29, 30*).

Over wavelengths from 0.5 to 1.5 μm, most of the surface has a blue (negative) spectral slope (*8, 9*), but some individual regions have a redder (flat to slightly positive) slope (Fig. 3E). Some individual boulders stand out in the spectral slope map, but not all boulders are redder than average; some are bluer (steeper negative slope). These data agree with photometric color

observations at higher spatial resolution, which show that individual boulders and craters have a variety of colors (*30*). Many of the areas that are redder than average occur at low latitudes, in agreement with some ground-based measurements that find equatorial reddening, though the measured variation in slope in OVIRS data is much smaller than is seen in those studies (*31*). As with the 3.4-μm absorption, the range of spectral behavior observed on Bennu at wavelengths shorter than 2.5 μm is similar to that found among B-type asteroids throughout the main belt (*5*). Bennu's blue color may be in part due to space weathering (*30*).

To determine whether Bennu's global characteristics are correlated at low spatial resolution, we calculated Spearman's rank correlation values, *r*, on different map pairs. We limited the calculation to latitudes less than 50° to avoid effects from variable solar illumination on short wavelength and thermal parameters, which affect high latitudes more strongly; at this limit, the temperature map has weak correlation to incidence or emission angles ($|r| < 0.25$), and further narrowing the latitude range did not meaningfully affect the results. At low phase angle, maps of the 2.74-μm hydration band depth and 0.55-μm reflectance show some correlation with peak surface temperature ($|r| = 0.76$ and 0.65, respectively) (Fig. S3) (*24*). The slope from 0.5 to 1.5 μm shows the least correlation with peak temperature, with the bluest and the reddest regions both being warmer than the average. However, spectral slope does weakly correlate with the hydration band and 0.55-μm reflectance ($|r| > 0.55$), with the reddest large boulders having the shallowest hydration band and the lowest reflectance.

Although the 3.2 to 3.6-μm band area map shows some boulders have a deeper absorption than others, comparison with other surface parameters (*24*) indicates no obvious correlation, and all map pairs have $|r| \leq 0.45$. Bennu's carbon band area follows neither the reddest nor the darkest regions on the surface. This is unexpected if Bennu's 3.4-μm band were attributable entirely to organics (*32*). However, as most spectra have an absorption shape that matches a mix of organics and carbonates (*28*), we cannot globally map these independently of one another. Thus, the lack of correlation may be the result of composition or for another reason, such as particle size effects.

As the 0.55-μm albedo and hydration band depth are correlated with surface temperature, we also produced a detrended 2.74-μm hydration band map (Fig. S4) to search for residual variations after removing the temperature dependence (*24*). Neither the band area from 3.2 to 3.6 μm, nor the spectral slope from 0.5 to 1.5 μm, show any correlation with the detrended hydration map, with $|r| \leq 0.23$ (*24*). The 2.74-μm hydration band map, caused by the presence of hydrated phyllosilicates, shows a correlation with latitude, $|r|=0.58$ (Fig. S5). This correlation decreases to $|r| = 0.48$ in the temperature-detrended map. The correlations between hydration band and peak surface temperature or latitude could be due to dehydration, differential space weathering, compositional differences, particle size/surface roughness, or other causes. Although hydrated phyllosilicates and carbon-bearing material are both globally present, their lack of correlation indicates separate formation processes.

Local variability

At the 20- to 30-m spot scale used in the global maps, spot-to-spot variability in band area (0.04 ± 0.01 to 0.84 ± 0.02 % μm) indicates a heterogeneous surface, either in terms of band depth or

shape. At the 5- to 10-m scale, the band shape and area are consistent over small areas where the spots overlap on a geologic feature (Fig. 4B), but change as the spots move to adjacent rocks, possibly due to local variability (Fig. 4A and 4C). However, some of these high spatial resolution data were acquired at phase angles where shadows may affect the signal, particularly at high latitudes or near large boulders (Fig. 4A).

Nonetheless, at the finer spatial scale absorption depths exceed 10% in a few isolated locations; these locations with the deepest absorptions likely have the highest concentration of carbon-bearing material, though viewing conditions and particle size effects may also affect band depth. Although full global coverage was not obtained at this resolution, 187 spectra (~1% of the high-spatial-resolution spots) were found to have absorptions of 5 to 14% at 3.42, 3.45, or 3.47 μm; these wavelengths were chosen to span the deepest absorption wavelengths for a mix of organics and carbonates (*28*). Most of these locations occur over boulders; only a single spectrum with a deep absorption feature occurs over a smooth crater floor, which is ringed by boulders having deep absorptions. However, this region is at high latitude, and the viewing conditions included some large shadows.

To avoid potential effects on band depth caused by shadows and low signal, we identified 18 low-latitude spectra with a 3.4-μm absorption feature >5% in depth and overlaid them on the OCAMS map of Bennu (*26, 27*). In some instances, the spots overlap spatially, resulting in 10 individual locations with deep 3.4-μm absorption (Fig. 5A). All of these locations lie on large boulders that dominate the OVIRS field of view. As with the global scale maps, these boulders span a range of brightness and colors, with no distinguishing morphological features; some appear buried or are composites of broken material, whereas others are neither (*30*). Another low-latitude region (Fig. 5B) shows that the deepest absorptions occur in a rock field between two craters. In comparison, the OSIRIS-REx mission's primary sample site, Nightingale crater at 56° N, 42° E (Fig. 5C), shows many spots with 3.4-μm absorption of 5 to 7% depth, even though the solar illumination is low. Again, most spots with deep features correspond to boulders around the rim of the crater, though there is an absorption over the entire region (*28*).

Origin of carbon material

The variation in 3.4-μm feature shape depends on surface location, with individual spot spectra that match other C-complex asteroids (Fig. 1A), demonstrating a heterogeneity that spans multiple asteroid families and classes. This heterogeneity is likely caused by varying proportions of carbonate and organics (*28*), which we cannot distinguish in our global data set. A spectral feature we observe at 3.98 μm may be due to carbonates (*28*) (Fig. 6), but the signal-to-noise ratio of the thermal-corrected spectra is <25 above 3.7 μm (*24*). An observed 2.3-μm feature could also be due to carbonates or to phyllosilicates, but the lack of a corresponding 2.5-μm absorption makes an identification uncertain. Spectral slopes could be affected by the presence of organics (*33*), but Bennu's spectral slope variation is small and redder OVIRS spectra show similar absorption features to bluer spectra in the low resolution 600 m^2 data (Fig. 6).

We do not observe widespread evidence of a 3.1-μm absorption from water ice or ammoniated phyllosilicates (Fig. 1B), which is present on many C-complex main-belt asteroids (e.g., Ceres, Themis) (*18, 22*), indicating that Bennu's bulk mineralogy and chemistry are distinct, despite the similarities in the 3.4-μm region. As a rubble-pile near-Earth asteroid, Bennu is a mixture of

parent-body material aggregates that have been warmed by proximity to the Sun, which would have removed volatile water ice (*34*).

Local regions on Ceres have complex mineralogy including organic matter, carbonates, and ammoniated phases (*33, 35*). Ground-based observations of Ceres indicated the presence of carbonates, whilst orbital data showed several organic-rich areas (*32, 36*). The limited spatial concentration of aliphatic organics on Ceres has been attributed to geologically recent exposure of those materials, such that they have not been broken down by solar irradiation (*33, 35, 37*). With irradiation, aliphatic carbon breaks down to graphitized or amorphous carbon, and these phases are thought to be ubiquitous on Ceres (*38*); they may also be present on Bennu (*29*) but cannot be directly observed with near-infrared spectroscopy. The widespread presence of aliphatic organics at 3.4 μm would indicate that neither space weathering nor heating on Bennu were pervasive enough to degrade (or graphitize) all aliphatic organics. To preserve a widespread 3.4-μm organic feature, most of the material on Bennu's surface cannot have been exposed to the space environment for more than a few million years (*39-41*).

Two scenarios could explain the carbon-bearing material on Bennu's surface and its variety of spectral shapes: accretion of external material over time or gradual exposure of a mix of materials present from its aggregation. First, given the similarity of local area spectral shapes to different C-complex asteroids, Bennu's surface may exhibit a mix of materials accreted during its time in the main belt and later transit to a near-Earth orbit. Pyroxene-bearing boulders have been detected on the surface and are spectrally consistent with the Howardite, Eucrite, and Diogenite (HED) achondrite meteorite groups associated with asteroid (4) Vesta (*42*), indicating that the surface retains at least some exogenous material. However, at the scale of these observations (~20 m per spot), there is no obvious connection between the carbon-bearing absorption features and any particular rock type (*30*). The meteorites that are the closest spectral analogs to Bennu (CI and CM chondrites) tend to have less than 5 vol% carbonates. Carbon-bearing materials were likely ubiquitous in the forming solar system and interstellar medium, so would have been available to form organics and carbonates in planetesimals (*43*). Any such material delivered to the surface of Bennu would be altered by space weathering and high surface temperatures, especially during perihelion, so pristine carbon-bearing material, particularly organics, would not be preserved unless synthesized and delivered in the last million years (*39-41*). The widespread distribution of such material on Bennu's surface makes this scenario unlikely.

Alternatively, as a rubble pile formed after a collision (*2, 25*), Bennu's surface may be peppered with boulders aggregated from different layers of its parent body and/or the impactor. Again, any surface materials, especially organics, would degrade over time. It is possible that buried organic material is being newly exposed by surface impacts, although we do not observe any correlation between the carbon-bearing material and craters (Figs. 3 and 5).

In the carbon-bearing boulders, thermal cycling and impact degradation by meteoroid impacts could cause fatigue and fracturing that exposes new organic material over time (*44, 45*). The ejection of particles from Bennu's surface supports the idea that fresh surfaces are actively being exposed (*46*). Bennu's blue spectral slope is also consistent with the colors of a subset of asteroids that show evidence of ongoing mass loss and are known as main-belt comets. However, on Bennu, this blue spectral slope extends to the shortest wavelengths we observe,

which is rare for main-belt comets (*19*). Conversely, some of Bennu's boulders display veins that may be composed of carbonate minerals (*28*), lending further credence to the supposition that we are observing a mixture of carbon-bearing materials.

Our observations provide context for the sample planned to be returned to Earth by OSIRIS-REx. The widespread surface distribution of the 3.4-µm absorption on Bennu indicates that the sample should contain carbon-bearing material, regardless of sampling location. The primary sample site, Nightingale, shows deeper regional carbon-bearing absorptions than average, particularly in the boulders around the crater rim; this does not rule out substantial carbon-bearing material on the crater floor.

References and Notes:

1. D.N. DellaGiustina, J.P. Emery, D.R. Golish, B. Rozitis, C.A. Bennett, K.N. Burke, et al., Properties of rubble-pile asteroid (101955) Bennu from OSIRIS-REx imaging and thermal analysis. *Nature Astronomy* **3**, 341-351 (2019).

2. D.S. Lauretta, A.E. Bartels, M.A. Barucci, E.B. Bierhaus, R.P. Binzel, W.F. Bottke, et al., The OSIRIS-REx target asteroid (101955) Bennu: Constraints on its physical, geological, and dynamical nature from astronomical observations. *Meteoritics and Planet Sci*. **50**, 834-849 (2015).

3. D.J. Tholen, Asteroid Taxonomy from Cluster Analysis of Photometry, Ph.D. Thesis, University of Arizona, Tucson (1984)

4. S.J. Bus and P.R. Binzel, Phase II of the Small Main-Belt Asteroid Spectroscopic Survey, A Feature-Based Taxonomy. *Icarus* **158**, 146-177 (2002).

5. J. de León, N. Pinilla-Alonso, H. Campins, J. Licandro, G.A. Marzo, Near-infrared spectroscopic survey of B-type asteroids: Compositional analysis. *Icarus* **218**, 196-206 (2012).

6. D.S. Lauretta, S.S. Balram-Knutson, E. Beshore, W.V. Boynton, C. Drouet d'Aubigny, D.N. DellaGiustina, et al., OSIRIS-REx: Sample Return from Asteroid (101955) Bennu. *Space Science Reviews* **212**, 925-984 (2017).

7. B.E. Clark, J. Ziffer, D. Nesvorny, H. Campins, A.S. Rivkin, T. Hiroi, et al., Spectroscopy of B-type asteroids: Subgroups and meteorite analogs, *J. Geophys. Res*., **115**, E06005 (2010)

8. B.E. Clark, R.P. Binzel, E.S. Howell, E.A. Cloutis, M.E. Ockert-Bell, P.R. Christensen, et al., Asteroid (101955) 1999 RQ36: Spectroscopy from 0.4 to 2.4µm and meteorite analogs. *Icarus* **216**, 462–475 (2011).

9. V.E. Hamilton, A.A. Simon, P.R. Christensen, D.C. Reuter, B.E. Clark, M.A. Barucci, et al., Evidence for widespread hydrated minerals on asteroid (101955) Bennu. *Nature Astronomy* **3**, 332-340 (2019).

10. W.F. Bottke, D. Vokrouhlický, K.J. Walsh, M. Delbo, P. Michel, D.S. Lauretta, et al., In Search of the Source of Asteroid (101955) Bennu: Applications of the Stochastic YORP Model. *Icarus* **247**,191-217 (2015).

11. H. Campins, A. Morbidelli, K. Tsiganis, J. de Leon, J. Licandro, D. Lauretta, The Origin of Asteroid 101955 (1999 RQ36). *Astrophysical Journal Letters* **721**, L53-L57 (2010).

12. N. Pinilla-Alonso, J. de León, K.J. Walsh, H. Campins, V. Lorenzi, M. Delbo, et al., Portrait of the Polana-Eulalia family complex: Surface homogeneity revealed from near-infrared spectroscopy. *Icarus* **274**, 231-248 (2016)

13. S. Sugita, R. Honda, T. Morota, S. Kameda, H. Sawada, E. Tatsumi, et al., The geomorphology, color, and thermal properties of Ryugu: Implications for parent-body processes. *Science* **364**, eaaw0422 (2019).

14. K. Kitazato, R.E. Milliken, T. Iwata, M. Abe, M. Ohtake, S. Matsuura, et al., The surface composition of asteroid 162173 Ryugu from Hayabusa2 near-infrared spectroscopy. *Science* **364,** 272-275 (2019).

15. H. Campins, J. de León, J. Licandro, M.S. Kelley, Y. Fernández, J. Ziffer, D. Nesvorný, Spectra of asteroid families in support of Gaia. Planetary and Space Science 73, 95-97 (2012)

16. D.C. Reuter, A.A. Simon, J. Hair, A. Lunsford, S. Manthripragada, V. Bly, et al., The OSIRIS-REx Visible and InfraRed Spectrometer (OVIRS): Spectral Maps of the Asteroid Bennu. *Space Science Reviews* **214**, 54 (2018).

17. B. Hapke, "Thermal Emission and Emission Spectroscopy," in *Theory of Reflectance and Emittance Spectroscopy* (Cambridge University Press, Cambridge, ed. 2012), pp. 412-439.

18. A. Rivkin, J. Emery, Detection of ice and organics on an asteroidal surface. *Nature* **464,** 1322–1323 (2010).

19. H. Campins, K. Hargrove, N. Pinilla-Alonso, E. Howell, M. Kelley, J. Licandro, T. Mothé-Diniz, J. Ziffer, Water ice and organics on the surface of the asteroid 24 Themis. *Nature* **464**, 1320-1321. (2010)

20. A.S. Rivkin, E.S. Howell, J.P. Emery, Infrared Spectroscopy of Large, Low-Albedo Asteroids: Are Ceres and Themis Archetypes or Outliers? *J. Geophys. Res Planets* **124**, 1393-1409 (2019).

21. A.S. Rivkin, E.L. Volquardsen, B.E. Clark, The surface composition of Ceres: Discovery of carbonates and iron-rich clays. *Icarus* **185**, 563-567 (2006)

22. F. Usui, S. Hasegawa, T. Ootsubo, T. Onaka (2019). AKARI/IRC near-infrared asteroid spectroscopic survey: AcuA-spec. *Publications of the Astronomical Society of Japan* **71**, 1-41 (2019).

23. P.R. Christensen, V.E. Hamilton, G. L. Mehall, D. Pelham, W. O'Donnell, S. Anwar, et al., The OSIRIS-REx Thermal Emission Spectrometer (OTES) Instrument. *Space Science Rev*. **214**, 87 (2018).

24. Materials, methods, and related figures are available as supplementary materials.

25. O.S. Barnouin, M.G. Daly, E.E. Palmer, R.W. Gaskell, J.R. Weirich, C.L. Johnson, et al., Shape of (101955) Bennu indicative of a rubble pile with internal stiffness. *Nature Geosci*. **12**, 247-252 (2019).

26. B. Rizk, C. Drouet d'Aubigny, D. Golish, C. Fellows, C. Merrill, P. Smith, et al., OCAMS: The OSIRIS-REx Camera Suite. *Space Sci. Rev*. **214,** 26 (2018).

27. C.A. Bennett, D.N. DellaGiustina, K.J. Becker, T.L. Becker, K.L. Edmundson, D.R. Golish, et al., A high-resolution global basemap of (101955) Bennu. *Icarus* 10.1016/j.icarus.2020.113690 (2020).

28. H.H. Kaplan, D.S. Lauretta, A.A. Simon, V.E. Hamilton, E.R. Jawin, R. Hanna, et al., Carbonates, Veins, and Alteration History of Asteroid (101955) Bennu. *Science, this collection.*

29. B. Rozitis, A. J. Ryan, J.P. Emery, P.R. Christensen, V.E. Hamilton, A.A. Simon, et al., Asteroid (101955) Bennu's Weak Boulders and Thermally Anomalous Equator. *Science Advances, this collection.*

30. D.N. DellaGiustina, K.N. Burke, K.J. Walsh, D.R. Golish, P.H. Smith, E.B. Bierhaus, et al., Diverse Color and Reflectance of Asteroid (101955) Bennu. *Science, this collection.*

31. R.P. Binzel, F.E. DeMeo, B.J. Burt, E.A. Cloutis, B. Rozitis, T.H. Burbine, et al., Spectral slope variations for OSIRIS-REx target Asteroid (101955) Bennu: Possible evidence for a fine-grained regolith equatorial ridge. *Icarus* **256**, 22-29 (2015)

32. C.M. Pieters, A. Nathues, G. Thangjam, M. Hoffmann, T. Platz, M.C. de Sanctis, et al., Geologic constraints on the origin of red organic-rich material on Ceres. *Meteoritics and Planetary Science* **53**, 1983-1998 (2018).

33. H.H. Kaplan, R.E. Milliken, C.M.O'D Alexander, New Constraints on the Abundance and Composition of Organic Matter on Ceres. *Geophys. Res. Letters* **45**, 5274-5282 (2018).

34. B Rozitis, J.P. Emery, M.A. Siegler, H.C.M. Susorney, J.L. Molaro, C.W. Hergenrother, et al., Implications for ice stability and particle ejection from high-resolution temperature modeling of asteroid (101955) Bennu. *J. Geophys. Res. Planets,* 10.1029/2019JE006323 (2020).

35. M.C. De Sanctis, V. Vinogradoff, A. Raponi, E. Ammannito, M. Ciarniello, F.G. Carrozzo, et al., Characteristics of organic matter on Ceres from VIR/Dawn high spatial resolution spectra. *Monthly Notices of the Royal Astro Soc*. **482**, 2407-2421 (2019).

36. M.C. De Sanctis, E. Ammannito, H.Y. McSween, A. Raponi, S. Marchi, F. Capaccioni, et al., Localized aliphatic organic material on the surface of Ceres. *Science* **355**, 719-722 (2017).

37. S. Marchi, A. Raponi, T.H. Prettyman, M.C. De Sanctis, J. Castillo-Rogez, C.A. Raymond, et al., An aqueously altered carbon-rich Ceres. *Nature Astronomy* **3**, 140-145 (2019).

38. A.R. Hendrix. F. Vilas, J-Y. Li, Ceres: Sulfur deposits and graphitized carbon. *Geophys. Res. Letters* **43**, 8920-8927 (2016).

39. B.E. Clark, B. Hapke, C. Pieters, D. Britt, "Asteroid Space Weathering and Regolith Evolution," in *Asteroids III* (University of Arizona Press, Tucson, 2002), pp. 585-599.

40. R. Brunetto, M.J. Loeffler, D. Nesvorný, S. Sasak, G. Strazzulla, "Asteroid surface alteration by space weathering processes," in *Asteroids IV* (University of Arizona Press, Tucson, 2015), pp. 597–616.

41. C.M. Pieters, S.K. Noble, Space weathering on airless bodies. *J. Geophys. Res*. **121**, 1865-1884 (2016).

42. DellaGiustina, D.N., H.H. Kaplan, A.A. Simon, W.F. Bottke, C. Avdellidou, M. Delbo, et al., Exogenic Basalt on Asteroid (101955) Bennu. *Nature Astronomy*, 10.1038/s41550-020-1195-z (2020).

43. F.J. Ciesla, S.A. Sandford, Organic synthesis via irradiation and warming of ice grains in the solar nebula. *Science* **336**, 453-454 (2012).

44. J.L. Molaro, S. Byrne, J.-L. Le, Thermally induced stresses in boulders on airless body surfaces, and implications for rock breakdown. *Icarus* **294**, 247-261(2017).

45. J.L. Molaro, K.J. Walsh, E. R. Jawin, R.-L. Ballouz, C. A. Bennett, D. N. DellaGiustina, et al., In situ evidence of thermally induced rock breakdown widespread on Bennu's surface. *Nature Communications* 11, 2913 (2020).

46. D.S. Lauretta, C.W. Hergenrother, S.R. Chesley, J.M. Leonard, J.Y. Pelgrift, C.D. Adam, et al., Episodes of particle ejection from the surface of the active asteroid (101955) Bennu. *Science* **366**, 6470 (2019).

47. P.R. Christensen, E. Engle, S. Anwar, S.L. Dickenshied, D.D. Noss, N. Gorelick, et al., JMARS – A Planetary GIS. American Geophysical Union Fall Meeting, San Francisco, CA, 2009. https://ui.adsabs.harvard.edu/abs/2009AGUFMIN22A..06C/abstract

48. D.C. Reuter, A.A. Simon, A. Lunsford, D.S. Lauretta, Origins, Spectral Interpretation, Resource Identification, Security, Regolith Explorer (OSIRIS-REx): Visible and InfraRed Spectrometer (OVIRS) Bundle. NASA Planetary Data System, https://sbn.psi.edu/pds/resource/orex/ovirs.html (2019).

49. A.A. Simon, D.C. Reuter, N. Gorius, A. Lunsford, G. Wind, R.G. Cosentino, et al., In-flight Calibration and Performance of the OSIRIS-REx Visible and IR Spectrometer (OVIRS). *Remote Sensing* **10**, 1486 (2018).

50. H.H. Kaplan, V.E. Hamilton, E.S. Howell, S.F. Anderson, M.A. Barrucci, J. Brucato, et al., Visible–Near Infrared Spectral Indices for Mapping Mineralogy and Chemistry with OSIRIS-REx. *Meteoritics and Planetary Science,* 10.1111/maps.13461 (2020).

51. B. Hapke, Bidirectional reflectance spectroscopy: 1. Theory. *J. Geophys Res. – Solid Earth* **86,** 3039-3054 (1981).

52. D.R. Golish, D.N. DellaGiustina, J.-Y. Li, B.E. Clark, X.D. Zou, P.H. Smith, et al., Disk-resolved photometric modeling and properties of asteroid (101955) Bennu. *Icarus*, 10.1016/j.icarus.2020.113724 (2020).

Acknowledgments: We are grateful to the entire OSIRIS-REx Team for making the encounter with Bennu possible and to C.W.V. Wolner for editorial review. We thank the developers of the JMARS open source software (https://jmars.mars.asu.edu/open_source) for assistance with Bennu-specific visualization (*47*). **Funding:** A.A.S., H.H.K., V.E.H., D.S.L., H.C., J.P.E. D.C.R., D.N.D., S.A.S., D.R.G., L.L. A.R, and C.A.B were supported by NASA under Contract

NNM10AA11C issued through the New Frontiers Program. B.R. acknowledges funding support from the Royal Astronomical Society (RAS) and the UK Science and Technology Facilities Council (STFC). **Author contributions:** All authors contributed to this manuscript by investigation (A.A.S., D.S.L., D.C.R., V.E.H., H.H.K.), data validation (A.A.S., D.C.R., V.E.H., D.R.G.), data curation (A.A.S., D.C.R., H.H.K., V.E.H., D.R.G., D.N.D., C.A.B.), conceptualization (A.A.S., D.S.L., D.C.R., V.E.H., H.H.K., J.P.E., A.R., B. R., M.A.B., L.L., S.A.S.), methodology (A.A.S., D.S.L., D.C.R., V.E.H., H.H.K., J.P.E., B. R., M.A.B., L.L., S.A.S.), formal analysis (A.A.S., H.H.K., V.E.H), and writing or editing (A.A.S., H.H.K., V.E.H., D.S.L., H.C., J.P.E. D.C.R., D.N.D., S.A.S., D.R.G., L.L. A.R, B.R., M.A.B, C.A.B.) **Competing interests:** We declare no competing interests. **Data and materials availability:** All OVIRS spectral data from the Detailed Survey and Reconnaissance phases are available via the Planetary Data System at https://sbn.psi.edu/pds/resource/orex/ovirs.html (*48*). Full resolution maps, and their corresponding 1σ error maps, are available as ancillary data files (*24*)

Methods:

All OVIRS spectra were calibrated using an automated pipeline that converts raw counts to calibrated radiance units (W cm^{-2} μm^{-1} sr^{-1}) (*24, 49*). Prior to science analysis, each spectrum is resampled onto a common wavelength axis with 2-nm spectral resolution <2.4 μm and 5-nm resolution from 2.4 to 4.3 μm. These resampled spectra were then fitted with a model of a thermal tail, which was subtracted, then divided by the solar flux to produce reflectance spectra (*24*). Surface feature maps were constructed using a Lommel-Seeliger disk correction to remove latitudinal effects. For band depth and shape comparisons, the background continuum was removed using a model fitted to each spectrum (*24*).

Supplementary Materials:
Materials and Methods
Figs. S1 to S6
References (*49-52*)
Supplementary Text
Ancillary Data Files 1 to 6

Fig. 1. Comparison of 3.4-μm absorption features on main belt asteroids and multiple locations on Bennu. (**A**) C-complex asteroid spectra obtained at 15° to 30° phase angle (*22*) - except the (24) Themis data from (*18*) - each plotted with 1σ uncertainties. Curves are offset from 1.0 for clarity. (**B**) The OVIRS globally averaged Bennu spectrum at 9° phase angle shows a broad absorption feature of ~2% depth, extending from 3.2 to 3.6 μm. The solid line shows the spectrum smoothed with a 9-spectral channel width Gaussian. Spectra of individual locations on Bennu are also shown, the coordinates of each location labelled, and curves are offset from 1.0 for clarity. Uncertainties are smaller than the symbol size.

Fig. 2. Effect of local solar time (phase angle) and spatial scale on absorption feature shapes and depths. (**A**) Globally averaged spectra at 10:00 am (~30° phase), 12:30 pm (~9°), and 3 pm (45°) local solar time, and the mean across all three phase angles; hatching indicates the standard

error from the mean. (**B**) Regional-scale (~900 m^2) spectra at the same phase angles as the global spectra, and their mean with standard error (hatching). Points show the data and lines are after smoothing with a 9-spectral channel width Gaussian. (**C**) Average of 163 local spectra (blue) compared with a regional two-spectrum average (black) and their difference (red); spectra are plotted as Gaussian-smoothed curves (lines) with standard error (hatching). (**D**) Approximate areas covered by the observations shown in (C), but without vertical along-track smear, which improves the overlap between the regional (black empty circles) and local (blue filled circles) spectral spots.

Fig. 3. Global spectral maps of Bennu from the OVIRS observations taken at the 12:30 pm Equatorial Station. (**A**) Band area from 3.2 to 3.6 μm, showing absorption due to carbon-bearing materials. (**B**) 2.74-μm hydration band depth, (**C**) effective surface temperature, (**D**) 0.55-μm reflectance, and (**E**) spectral slope from 0.5 to 1.5 μm. The latitude and longitude grid shown in A is overlain on the other panels.

Fig. 4. Individual high-areal-resolution (~60 m^2) local spectra, and their corresponding OVIRS footprints. (A-C) Spectra of selected locations and their means. (D-F) The corresponding OVIRS footprints (ellipses, elongated by along-track motion) overlain on OCAMS panchromatic images acquired at the same time. In (**A**), a deep absorption feature changes spectral shape and depth as the field of view moves off a large boulder and onto smaller boulders (**D**), which could have different composition, and the mean shows variation over the full band. In (**B**), a cluster of spectra over a rock pile (**E**) shows consistent shapes with less variation in the mean than in (A). In (**C**), a region with little absorption shows few large boulders in the field of view (**F**) and similar variation in the mean as (B).

Fig. 5. The locations and sizes of OVIRS footprints (white outlines) of spectra with single-channel absorptions >5% at either 3.42, 3.45 or 3.47 μm. The footprints are overlaid on the 5-cm-resolution base map (*26, 27*); they are elongated by surface projection effects but neglect along-track smear. Footprint coverage over the images is sparse, primarily in separated north-south scans. (**A**) Low latitudes show a number of deep absorptions, primarily over boulders. (**B**) An adjacent equatorial region shows that the boulders between two craters also have deep absorptions. (**C**) The environs around the OSIRIS-REx primary sample site, Nightingale crater (dashed circle), also show locally deeper absorptions.

Fig. 6. Bennu reflectance spectra from 2 to 4 μm. The global average spectrum (black curve) shows other absorption features centered near 2.3 and 3.98 μm. There is little difference in the reflectance spectrum of any spot, regardless of spectral slope from 0.5 to 1.5-μm, with redder regions (red curve) showing the same spectral features as bluer regions (blue curve). The red and blue curves are shifted by 0.2 for clarity.

Science
AAAS

Supplementary Materials for

Widespread carbon-bearing materials on near-Earth asteroid (101955) Bennu

Amy A. Simon[1*], Hannah H. Kaplan[2], Victoria E. Hamilton[2], Dante S. Lauretta[3], Humberto Campins[4], Joshua P. Emery[5], M. Antonietta Barucci[7], Daniella N. DellaGiustina[3], Dennis C. Reuter[1], Scott A. Sandford[6], Dathon R. Golish[3], Lucy F. Lim[1], Andrew Ryan[3], Benjamin Rozitis[8], Carina A. Bennett[3]

This file includes:

Materials and Methods

Calibration to radiance units

To ensure that the spectral region from 3 to 4 μm had the required sensitivity, the OVIRS instrument was internally coated with an inorganic black anodize, precision-cleaned, and contamination-controlled during integration and testing with a dry nitrogen purge (*16*). In ground testing, each pixel was characterized spatially, spectrally, and radiometrically with National Institute of Standards and Technology traceable sources (*49*). The spatial response was validated with Earth/Moon flyby data; there is no spatial component across the field of view (i.e., with varying wavelength within a filter segment). During a spacecraft slew, there can be some difference in terrain viewed, but only in the filter segments on opposite ends of the detector due to ground-track motion during the readout. The wavelengths within the carbon band are all in the same filter (near its center and also near the center of the detector) and are read out simultaneously – they physically cannot see different terrain under any viewing conditions. In-flight performance has shown no changes in this spectral region, and spectra of other external targets and internal calibration sources are clean of any absorption at these wavelengths.

For these analyses, each OVIRS spectrum was calibrated using a standard pipeline process to convert from raw counts to physical radiance units; these data are delivered to the Planetary Data System (*48)*. All of the OVIRS data were acquired with onboard summing, but some used a minimal 2 pixels per "superpixel," and some used 8 pixels per superpixel to reduce the data volume. The ground calibration pipeline converts the raw superpixel data to physical units by i) subtracting the background level from adjacent deep space views, ii) adjusting for the numbers of pixels in the superpixels, iii) calculating and removing any out-of-band IR signal leakage (*49*), iv) converting to radiance units using conversion factors generated from both ground and flight calibration data, v) and screening cosmic rays (outliers 3σ from the mean at a given wavelength). The absolute radiometric accuracy is ~ ±2%, but the relative accuracy and precision are better than 1% (*49*).

Conversion to reflectance

Each calibrated radiance spectrum is resampled onto a common wavelength axis with 2-nm spacing below 2.4 μm and 5-nm spacing above 2.4 μm, removing any spectral overlap for ease of analysis. The thermal tail is then removed from each spectrum. Multiple methods were investigated for thermal tail removal: i) a single blackbody with a single emissivity, ii) a single blackbody with any emissivity scaling and a fixed slope, iii) an unscaled blackbody with a fit linear slope, iv) a Gaussian distribution of blackbody temperatures, and v) a Bayesian temperature-emissivity separation. After trials across several large OVIRS data sets, method ii) did the best job fitting the majority of the spectra and removing thermal radiance. Occasional bad thermal tail fits do occur, primarily at high phase angles, but they are obvious in the 1σ error maps and are excluded from any analyses.

To find the thermal radiance for each spectrum, a linear continuum model was fitted from 1 to 4 μm with a slope of 0.05 μm^{-1} (found by empirical fits to the data itself, which show little variance in radiance slope), multiplied by a range-corrected solar spectrum, and scaled to Bennu's radiance at ~2.1 μm (mean from 2.08 to 2.16 μm). This scaled solar radiance is subtracted from the OVIRS spectrum to find the remaining thermal radiance. The thermal radiance spectrum is

then fitted with a single temperature blackbody curve by computing the blackbody radiance every 1 K from 150 to 475 K, scaling to the measured thermal radiance, and minimizing the χ^2 goodness of fit. The best fitting models commonly have scale factors of 0.5 to 0.7. At the OVIRS long wavelengths the thermal radiance is dominated by the hottest temperatures within the OVIRS spot. Thus, the scale factor likely represents the fractional areal coverage of surface temperatures close to or above the derived temperature with the spot. While the scale factor does not represent a true emissivity, it is consistent with the terrain roughness or shadow coverage observed within a spot, *e.g.*, Fig 4. Because it is a best fitting model, all the thermal radiance is removed with this method regardless of the spectral slope (Fig. S2, A and B). By subtracting a smooth function, the thermal tail removal does not add noise to the spectrum, though it lowers the overall signal to noise ratio (SNR) particularly at the long wavelengths (Fig. S2, C). Internal instrument calibration source data acquired close in time were used to calculate SNR without any outlier screening or resampling applied, and then scaled to the Bennu signal level. At 3.4 μm, the SNR is about 50 after thermal tail removal.

The resulting thermal tail-removed radiance spectra are divided by the range-adjusted solar flux to produce reflectance spectra. We then screened each spectrum for large outliers (one standard deviation from a 5-channel mean) to remove residual noise spikes. We smoothed the spectra with a 9-spectral channel width Gaussian kernel; individual spectra in the figures show the unsmoothed data points, as well as the smoothed curves. To normalize any residual IR slope for band comparisons, each spectrum was divided by its continuum, which was fit with a quadratic function using the radiance at 2.95, 3.2, and 3.6 μm. Although this continuum model is arbitrary, we selected these wavelengths to avoid absorption bands of interest near 3.1 and 3.4 μm. Comparisons of models fitted at slightly different wavelengths showed no substantive effect on the overall spectral shape, and a quadratic model flattens the spectra better than a linear one. Although this fitting might slightly affect absorption band depths, it does not affect the spectral shapes, which are apparent in the original radiance and reflectance spectra.

To assess any remaining instrumental effects, we checked the same local areas for spectral consistency at the smallest spatial scales. An example scan shows some spectral inhomogeneity as the OVIRS spot crosses new boulders (Fig. 4A), but fully overlapping spots show spectral consistency (Fig. 4B). The same spectral shape is also observed with repeated coverage over time and at different phase angles. This consistency from observation to observation of an area at any spatial scale or phase angle provides us with confidence in the detection of the absorption band.

Mapping methodology

Mapped values, such as band depth, band area, and spectral slope, and the corresponding uncertainties on these values were calculated using the spectral parameterizations described below (*50*). Maps were produced both with and without a correction by a Lommel-Seeliger photometric disk function with no free parameters; this formulation has previously been used to describe the photometric behavior of low-albedo surfaces (*51, 52*). This disk correction accounts for the incidence and emission angle dependence of the OVIRS observations, but we do not include a phase function, as that varies by only a few degrees within a mapping sequence. For display purposes, Fig. 3 maps include the disk correction.

Organic/carbonate band area map values are the absorption area between 3.2 and 3.6 μm calculated on the continuum-removed spectra. The map value from each OVIRS spot is then projected onto the facetized shape model (*25*) and, where multiple spots overlap the same facet, the values are combined with a weighted average using the uncertainty as the weight. Uncertainties on each OVIRS spot map value are also combined on the facets to produce a 1σ standard error map (Fig. S6). We use a shape model with 196,608 facets; this method takes the ~20-m OVIRS spots and places them on the shape model with a resolution of ~3 m per facet side.

The maps shown in Fig. 3D and 3E use the wavelengths specified (i.e., linear spectral slope from 0.5 to 1.5 μm, or 0.55-μm reflectance). The hydration band depth, *BD*, map is calculated at 2.74 μm, the band minimum (*9*), and is measured from a linear continuum with endpoints at 2.6 and 3.0 μm. Other formulations of this band depth using continuum points at longer or shorter wavelength positions result in similar band depth values and spatial trends. The surface temperature map is derived from the thermal tail of the radiance spectrum from 3 to 4 μm, as described above. We find a correlation ($|r| = 0.76$) between the hydration band depth and surface temperature for latitudes within ±50°. To make the detrended hydration band map, we found the best fitting linear model to the trend between band depth and temperature, *T*, at all latitudes ($|r| = 0.79$) and subtracted it ($BD = 0.492 - 0.011T$). The Hayabusa2 team found a similar relationship between temperature and hydration band depth at C-type asteroid Ryugu and use a similar detrending approach (*14*).

Supplemental Text

Ancillary Data File Information

Full resolution versions of the OVIRS maps are available as ancillary Data Files in Flexible Image Transport System (FITS) format. Each file is composed of 6 columns: shape model facet number, latitude, longitude, facet radius, value, and 1σ uncertainty. File headers include additional data product information, including the map content. The files are: Data File 1 = carbon band area, Data File 2 = 2.74-μm hydration band depth, Data File 3 = temperature, Data File 4 = 0.55-μm reflectance, Data File 5 = 0.5 to 1.5-μm spectral slope, Data File 6 = temperature-detrended hydration band depth. Some small artifacts (e.g., filter segment jumps) remain in the OVIRS spectral data and can make their way into the maps. Every effort has been made to filter out bad values including values with abnormally high uncertainty. The suggested color stretch for these maps is mean value ± 2 standard deviations.

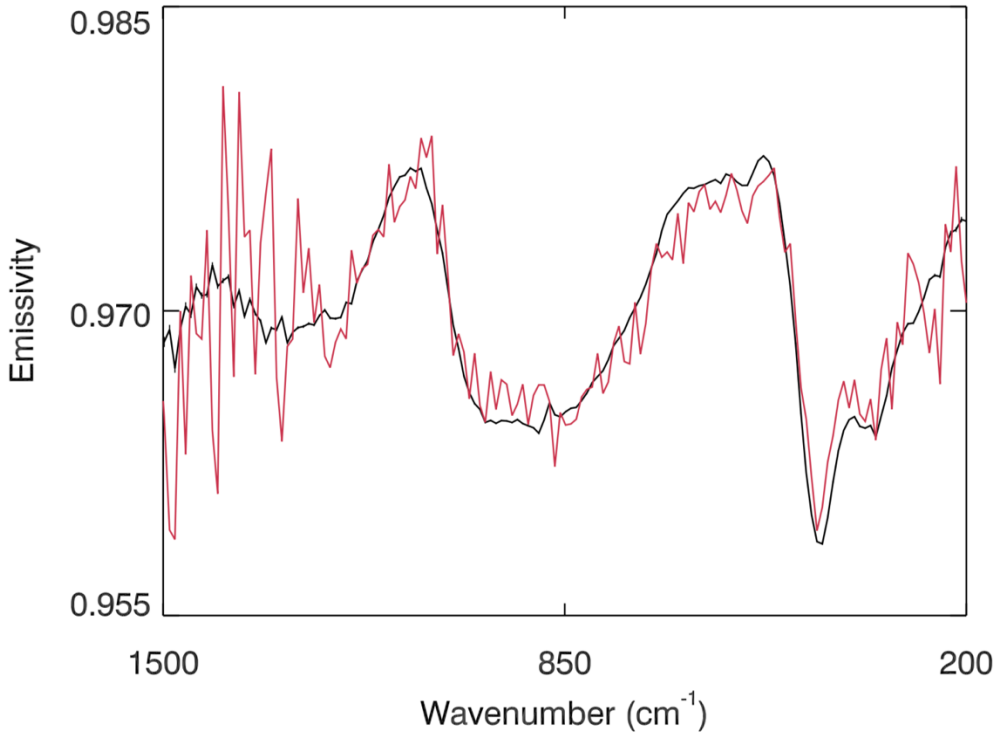

Fig. S1. OTES emission spectra of Bennu. The global average Bennu spectrum (black curve) shows good SNR (standard errors are the size of the line thickness). An individual OTES spectrum (red curve) does not have adequate SNR to search for the presence of carbonate or organic features.

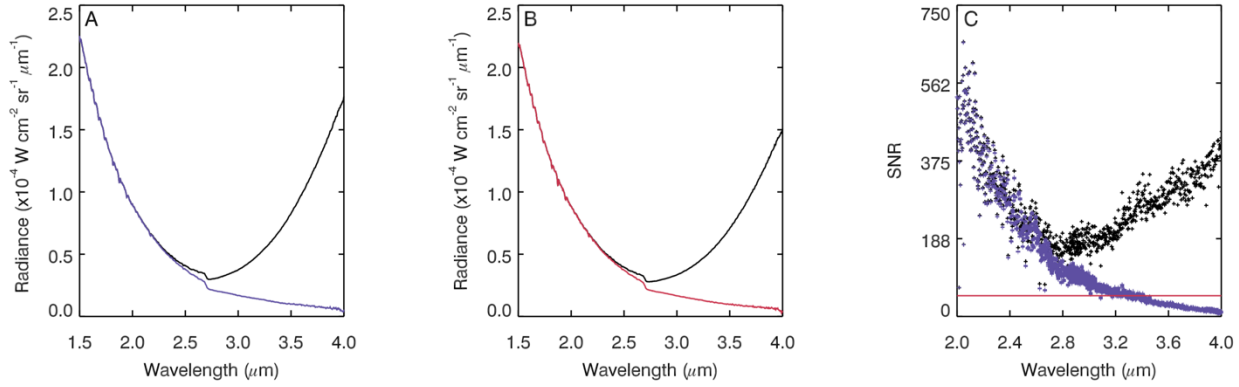

Fig. S2. Thermal tail removal and resulting signal-to-noise ratio. (**A**) A typical Bennu radiance spectrum, with and without thermal tail removal (blue and black curves, respectively). (**B**) A redder Bennu radiance spectrum, with and without thermal tail removal (red and black curves, respectively). (**C**) SNR at the pixel level (before resampling), for a typical Bennu spectrum with and without thermal tail removal (blue and black, respectively). SNR=50 is indicated by the line.

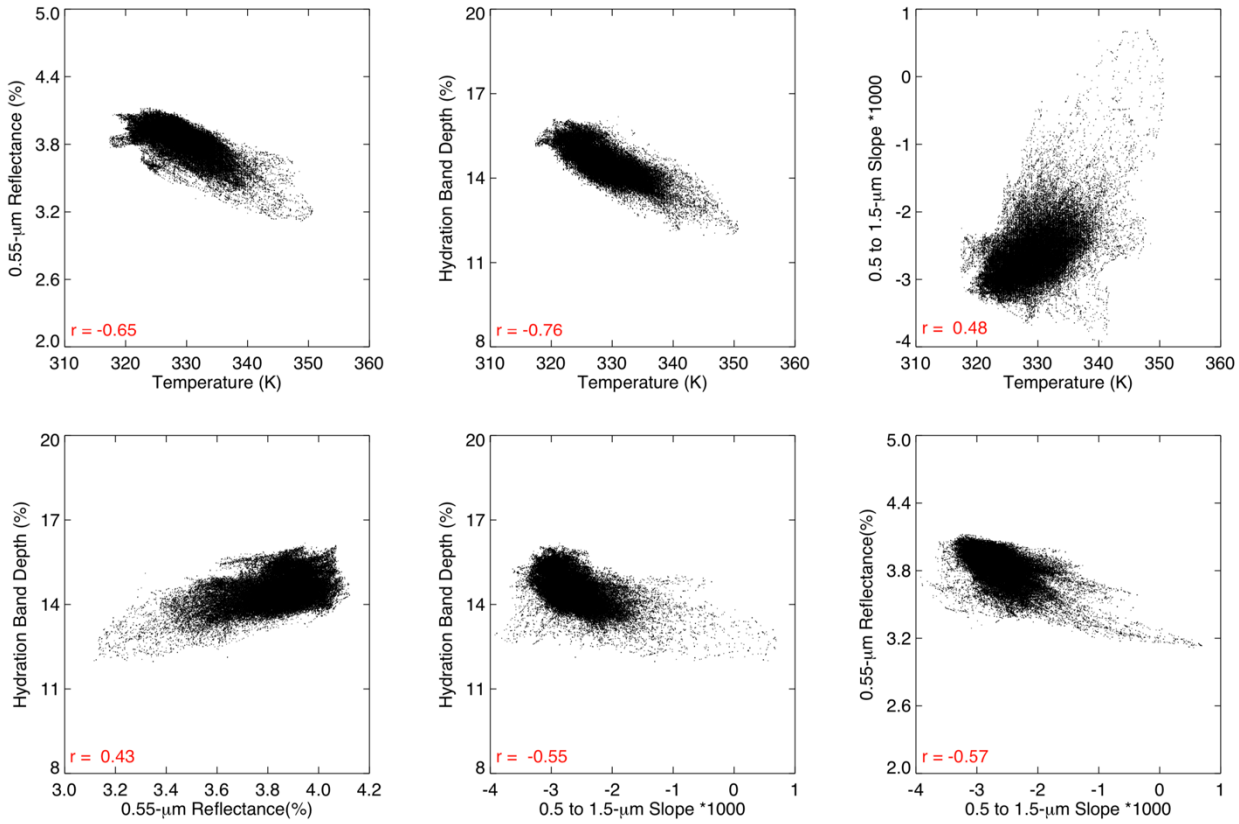

Fig. S3. Correlation plots for the map pairs shown in Fig. 3. Map pairs of 0.55-µm reflectance (Fig. 3D) vs. surface temperature (Fig. 3C), hydration band (Fig. 3B) vs. surface temperature (Fig. 3C), spectral slope (Fig. 3E) vs. surface temperature (Fig. 3C), 2.74-µm hydration band (Fig 3B) vs. reflectance (Fig. 3D), 2.74-µm hydration band (Fig 3B) vs. spectral slope (Fig. 3E), and 0.55-µm reflectance (Fig. 3D) vs. spectral slope (Fig. 3E). The Spearman's rank correlation coefficient is listed for each pairing.

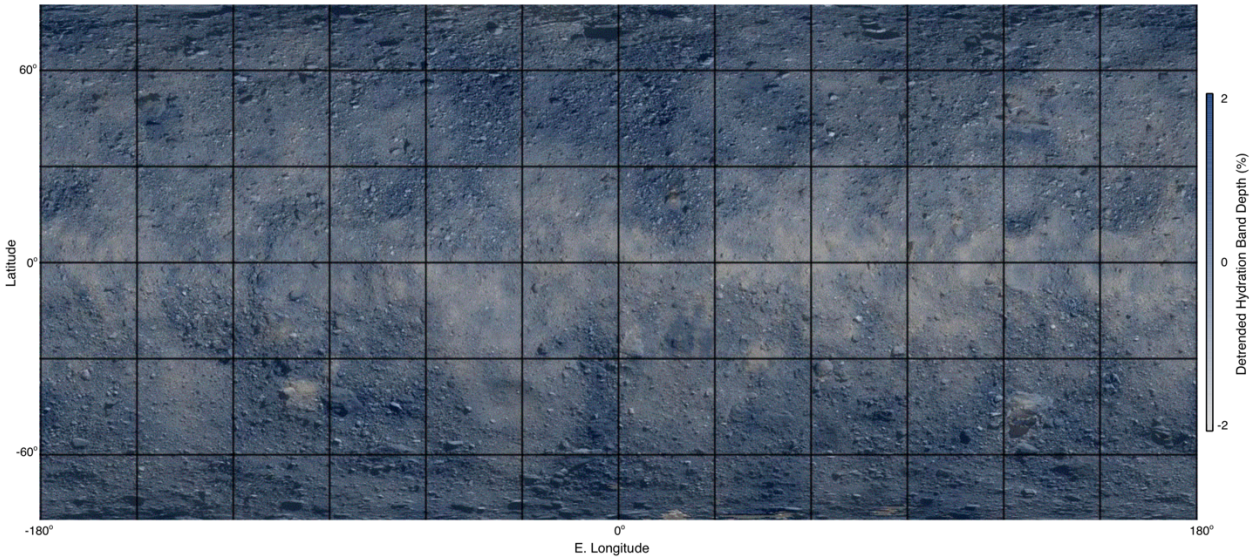

Fig. S4. Map of temperature-detrended hydration band depth. Hydration band map with temperature correlation removed, using the trend found in Fig. S3.

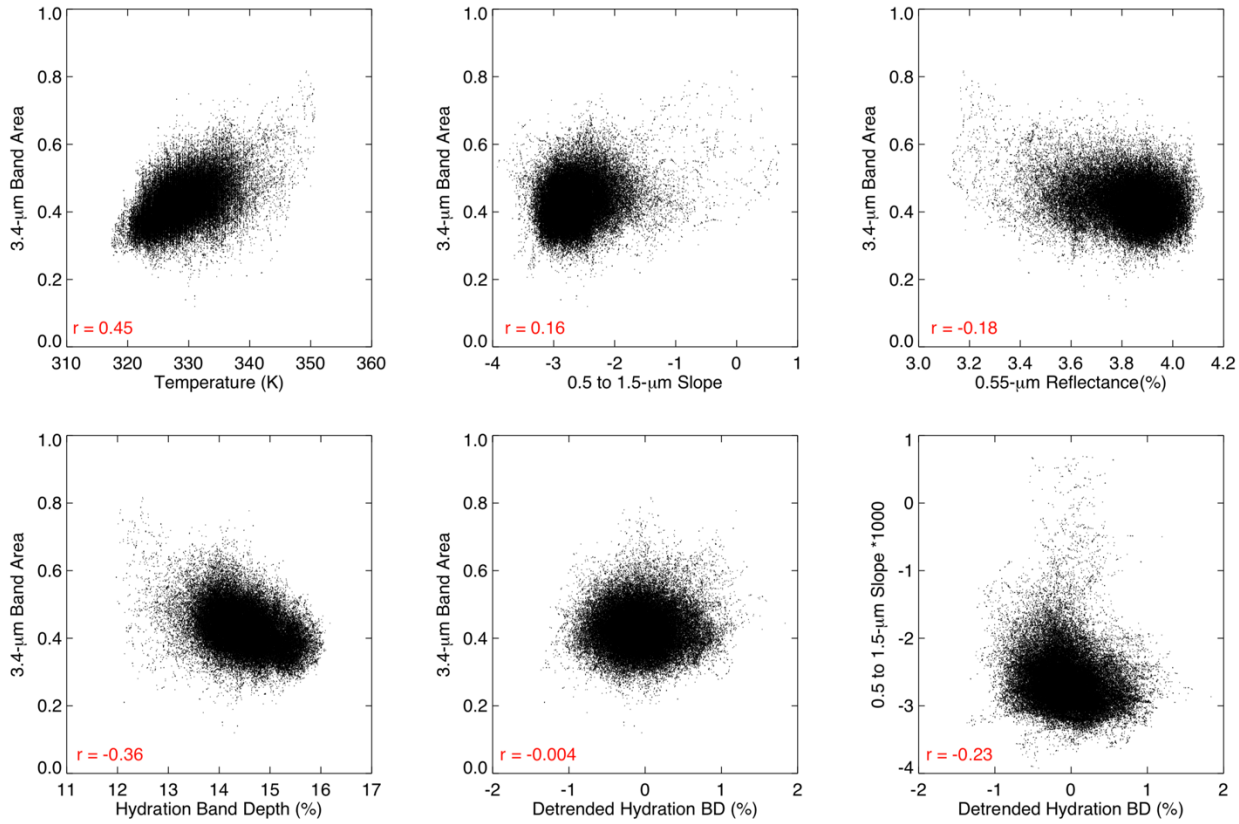

Fig. S5. Correlation plots for the 3.2 to 3.6-μm band area map. As in Fig. S3, but for map pairs of Fig. 3A vs. surface temperature (Fig. 3C), hydration band (Fig. 3B), reflectance (Fig. 3D), spectral slope (Fig. 3E), and temperature-detrended hydration band depth (Fig. S4) maps.

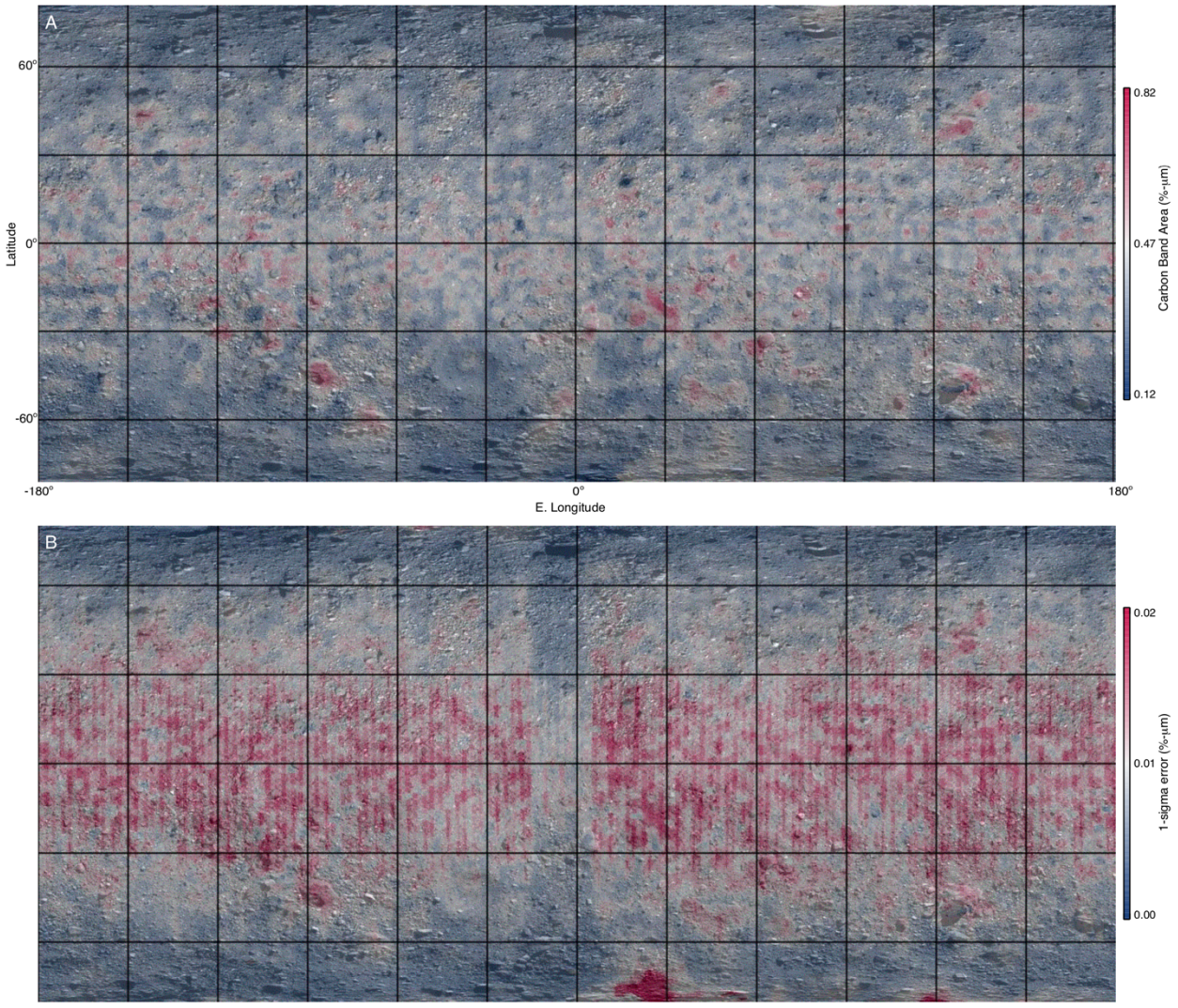

Fig S6. Carbon band area and error map for 3.2 to 3.6 µm at 12:30 pm. (**A**) Higher resolution version of the map shown in Fig. 3A. (**B**) The corresponding 1σ standard error map.